metals

MDPI

Article

Shear Transformation Zone and Its Correlation with Fracture Characteristics for Fe-Based Amorphous Ribbons in Different Structural States

Weiwei Dong *, Minshuai Dong, Danbo Qian, Jiankang Zhang and Shigen Zhu

College of Mechanical Engineering, Donghua University, Shanghai 201620, China
* Correspondence: wwddhush@dhu.edu.cn

Abstract: Fe-based amorphous alloys often exhibit severe brittleness induced by annealing treatment, which increases the difficulties in handling and application in the industry. In this work, the shear transformation zone and its correlation with fracture characteristics for FeSiB amorphous alloy ribbons in different structural states were investigated. The results show that the bending strain decreases sharply with the annealing temperature increase, accompanied by decreased shear band density and the induced plastic deformation zone. Furthermore, the microscopic fracture surface features transform from a micron-scale dimple pattern to nano-scale dimples and periodic corrugations. According to nano-indentation results, the strain rate sensitivity and shear transformation zone volume change significantly upon annealing treatment, which is responsible for the deterioration of bending ductility and the transition of microscopic fracture surface features.

Keywords: shear band; shear transformation zone; fracture surface; dimple pattern; periodic corrugations

check for updates

Citation: Dong, W.; Dong, M.; Qian, D.; Zhang, J.; Zhu, S. Shear Transformation Zone and Its Correlation with Fracture Characteristics for Fe-Based Amorphous Ribbons in Different Structural States. *Metals* **2023**, *13*, 757. https://doi.org/10.3390/met13040757

Academic Editors: Sundeep Mukherjee and Giovanni Meneghetti

Received: 26 February 2023
Revised: 1 April 2023
Accepted: 10 April 2023
Published: 13 April 2023

Copyright: © 2023 by the authors. Licensee MDPI, Basel, Switzerland. This article is an open access article distributed under the terms and conditions of the Creative Commons Attribution (CC BY) license (https://creativecommons.org/licenses/by/4.0/).

1. Introduction

FeSiB amorphous alloy ribbons are a widely used soft magnetic material, which is characterized by its simple preparation process, low production cost, and low loss rate. In addition, it exhibits excellent properties such as high magnetic permeability, low coercive force, and low iron core loss, making it widely applied in the iron cores of commercial high-efficiency distribution transformers, intermediate frequency (400–10,000 Hz) transformers, filters, inductors, and reactors. Therefore, optimizing the soft magnetic properties of FeSiB amorphous alloy ribbon is a hot research topic in this field. Among these, the annealing treatment of FeSiB amorphous alloy ribbon below the crystallization temperature is an effective method, which can further improve the soft magnetic properties of Fe-based amorphous alloys through structure relaxation. However, FeSiB amorphous alloy ribbon often suffers from severe annealing embrittlement, which affects its comprehensive properties, increases its processing and application difficulties in the industry, and has attracted high attention from the academic and industrial communities [1,2].

The plastic deformation mechanism of amorphous alloys is completely different from that of crystalline materials because the atomic arrangement of amorphous alloys exhibits short-range order and long-range disorder, and there are no crystal defects such as dislocations and grain boundaries. Therefore, the plastic deformation theory of traditional crystalline materials cannot be applied to amorphous alloys. Currently, the main theories of amorphous alloy deformation are the free volume theory and the shear transformation zone (STZ) theory. The free volume model is a phenomenological physical concept, which states that plastic deformation of amorphous alloys can be achieved under local atomic transition conditions. After annealing treatment, the free volume of amorphous alloys is eliminated due to the random jump motion of atoms, leading to the structural relaxation of amorphous alloys. The reduction in free volume after annealing decreases the plastic deformation ability of amorphous alloys [3,4]. However, the microstructural origin of

embrittlement caused by structural relaxation is not clear yet. Currently, a large amount of research has shown that the plastic deformation mechanism of amorphous alloys is closely related to shear bands. Shear bands are a typical feature of ductile banded amorphous alloys, which are generated when ductile bands start to bend, and their formation is related to the evolution of local structural order. When amorphous alloy ribbons have a large number of shear bands, it indicates that they have good bending ductility. In the plastic deformation process of amorphous alloys, the activation of STZs is an important step. The STZ theory states that the plastic deformation of amorphous alloys is not realized by the transition of single atoms but by clusters of atoms composed of numerous atoms as flow units, under certain conditions. STZ is a micro deformation area caused by local structural changes, and its size is usually between several nanometers to tens of nanometers. The activation of STZs in amorphous alloys is closely related to factors such as material composition, temperature, strain rate, and stress level [5–7]. Therefore, understanding the plastic deformation mechanism of amorphous alloys and the formation of shear bands has important academic value and practical significance for the development of high-performance amorphous alloy materials.

STZ has been widely employed to study the low-temperature deformation of amorphous alloys. However, the correlation between the measured STZ size and amorphous alloys ductility was also controversial. Particularly, Pan et al. [8,9] evaluated the STZs size in amorphous alloy by using the rate-change method. It was found that upon annealing, the measured STZ size dramatically decreases. The study demonstrates that amorphous alloy with larger STZ size enjoys better plasticity. Whereas someone held the opposite opinion that amorphous alloy with smaller STZ size possesses better plasticity. Ma et al. [10] employed statistical analysis of the maximum shear stress, which is based on the distribution of the first pop-in events in nanoindentation, to estimate the STZ volume and atoms it contains in the amorphous alloy. The result indicates that the STZ size decreases from 83 atoms in the ribbon to 36 atoms in the film. Upon nanoindentation creep test, STZ sizes with 44 atoms and 18 atoms were calculated for the ribbon and film, respectively. Choi et al. [11] employed statistical analysis of the data to estimate the STZ size. The results of the analysis indicate an STZ size of ∼25 atoms in amorphous alloy, which increases to ∼34 atoms upon annealing. The activation volume of a single STZ was estimated from either a statistical analysis or the rate-change method. The STZ size obtained by the rate-change method shows a better correlation with amorphous alloy plasticity [12,13].

In order to reveal the mechanism of brittleness for FeSiB amorphous alloy ribbons, this study was carried out. To investigate the relationship between shear transformation zone (STZ) size and bending ductility of FeSiB amorphous alloy ribbons, the FeSiB amorphous alloy ribbons were annealed at various temperatures. FeSiB amorphous alloy ribbons with different structural states were selected as the research objects. In this study, the STZ size was measured by the rate change method, and the bending toughness, folding morphology, and resulting fracture surfaces of FeSiB amorphous ribbons under different free volume states were further studied. The formation mechanism of shear bands and fracture surface characteristics were systematically discussed. The results showed that reducing the volume of STZs can effectively reduce the brittleness of FeSiB amorphous alloy ribbons, providing new ideas for improving the bending ductility of FeSiB amorphous alloys by controlling their structural states. Meanwhile, this study has important theoretical significance for a deeper understanding of the fracture behavior of amorphous alloys and its relationship with structural factors and can provide certain technical guidance for the development of high-performance amorphous alloys.

2. Materials and Methods

All materials used in this experiment are of high purity. The mass of each element was calculated based on the nominal composition of Fe80Si9B11, and the required raw materials were weighed using a high-precision electronic balance. Prior to melting the high-purity raw materials, titanium ingots were melted to absorb oxygen and impurities in the high-

vacuum arc furnace. The furnace vacuum degree was reduced to below 5×10^{-3} Pa and high-purity argon gas was introduced for protection during the melting process. Under the heating conditions of an induction coil, a mixture of pure Fe (99.9 mass%), Si (99.9 mass%), and FeB (17.9 mass%B) was melted to prepare an Fe80Si9B11 alloy ingot. The ingot was repeatedly melted four times and finally cooled for 30 min with furnace cooling to obtain a homogenous master alloy ingot. Before preparing the FeSiB amorphous alloy ribbons, the surface impurities of the master alloy ingot were thoroughly removed and subsequently shattered into small alloy ingots. The single-roller melt-spinning technique was used to prepare the amorphous alloy strip, which is easy to operate and has a fast cooling rate, making it possible to produce suitable amorphous alloy strips. The preparation process of the FeSiB amorphous alloy ribbons was carried out completely in a high-purity argon gas atmosphere, with an argon pressure differential of 0.02 MPa to ensure a stable atmosphere. The molten alloy was ejected from the narrow slit at the bottom of a quartz tube onto a rapidly rotating copper wheel, with a surface speed of 40 m/s, allowing for control of the thickness and width of the amorphous alloy ribbons. The ribbons were 25 ± 2 μm in thickness and 8 mm in width. The structure and morphology of the ribbons were examined using X-ray diffraction (XRD) with Co-Kα (λ = 1.7902 Å) under a step of 0.01° and a counting time of 4 s per step at 40 kV and 20 mA. The as-cast and annealed at 250 °C and 380 °C amorphous ribbons were labeled as S25, S250, and S380, respectively. The S250 and S380 ribbons were annealed at 250 and 380 °C for 90 min in a tubular vacuum furnace (<0.1 Pa) with furnace cooling, the heating rate was 10 °C/min. The bending ductility of ribbons was tested with a self-designed two-point bending device, which was composed of three boards. The schematic diagram of the two-point bending test is shown in Figure 1. The top and side boards were fixed, and the lower one could move from up and down. The ribbons were fixed on the upper and lower boards, and then the lower board was controlled to move up at the speed of 0.1 mm/s. The bending strain was used as ductility index λ_f to value the bending ductility of the ribbons [1], as Equation (1):

$$\lambda_f = \frac{t}{L_f - t} \tag{1}$$

where t is the ribbon's thickness, and L_f is the board spacing when the ribbons have just broken. The ribbons which could be folded at 180° without breaking down show good ductility.

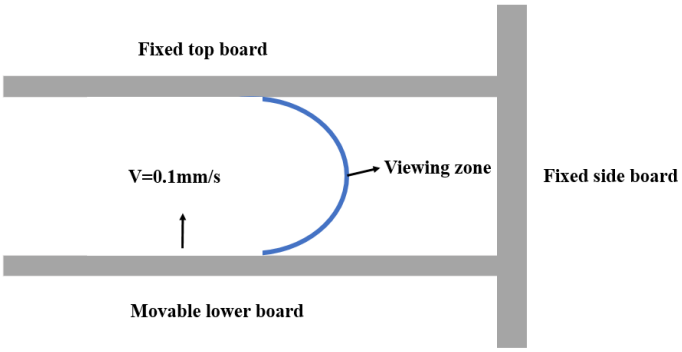


Figure 1. The schematic diagram of two-point bending test.

The macro and micro images of the bent crease and resultant fracture surface of these three samples were investigated by scanning electron microscopy (Field Emission Scanning Electron Microscope, FESEM, JSM-7500F, JEOL, Japan) and transmission electron microscope (TEM, JEM-2100, JEOL, Japan). The FeSiB amorphous alloy ribbons were subjected to nano-indentation testing (Agilent G200, Keysight, Santa Rosa, CA, USA) using a Berkovich diamond indenter with an effective tip radius of 25 nm. The experimental samples were mechanically polished to ensure that the surface of the FeSiB amorphous alloy ribbons was perpendicular to the loading direction of the indenter and tested in a

constant temperature and humidity as well as a quiet environment. The load was increased at rates of 0.01, 0.05, 0.1, and 0.2 mN/s. The nano-indentation test was conducted 10 times at various loading rates for each sample.

3. Results

Results and Discussion

As shown in Figure 2, the XRD patterns of as-cast and annealed FeSiB alloy samples S25, S250, and S380 exhibit broad peaks without any sharp diffraction peak related to the crystalline phase. This suggests that all the samples keep an amorphous structure.

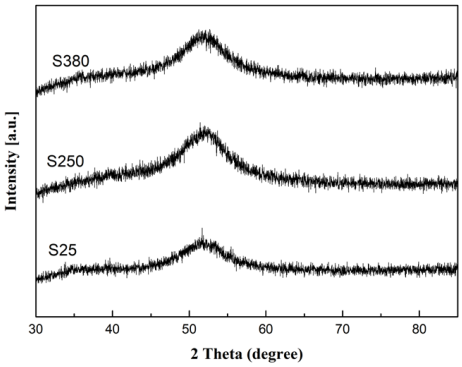


Figure 2. XRD patterns for amorphous alloy ribbons in different structural states: S25, S250, and S380.

In order to further confirm that the as-cast and annealed FeSiB amorphous alloy ribbons are amorphous, they were tested by HRTEM. Figure 3 shows the HRTEM images and corresponding selected area electron diffraction (SAED) patterns of S25 and S380. For the as-cast (Figure 3a) and annealed sample (Figure 3b), no precipitated nanometer-sized phase is detected, only the homogeneous mazy contrast and a diffuse halo are presented, This is a typical structural characteristic of amorphous alloys, which is consistent with XRD results, demonstrating that these three samples annealed at different temperatures still remain a monolithic amorphous structure.

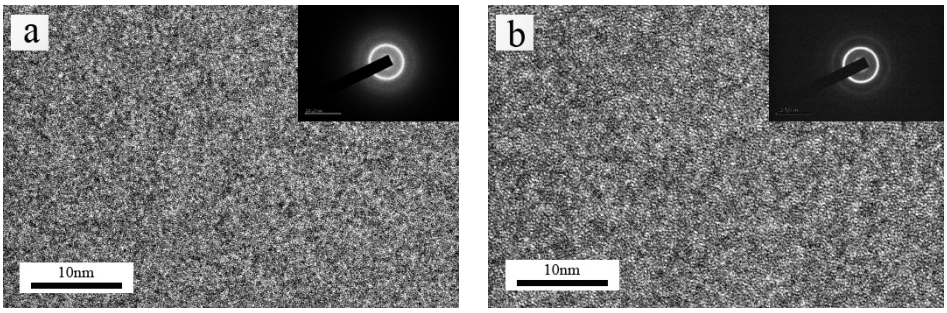


Figure 3. High-resolution TEM image inset with corresponding SAED pattern for (**a**) S25 and (**b**) S380.

It is well known that amorphous alloy is usually located in a metastable state, a structure relaxation would process this in a wide temperature range from room temperature to crystallization temperature. The exothermic event accompanied by structure relaxation shows that the amount of free volume in amorphous alloys is decreased. The exothermic enthalpy value is related to the free volume content,

$$\Delta H_{f_v} = \beta \cdot \Delta V_f \quad (2)$$

where ΔH is exothermic enthalpy, which is positive to the annealing temperature, ΔV_f is the change of free volume, β is a constant parameter [14]. In this study, for these three samples, the exothermic enthalpy values of samples S250 and S380 increase with the increase in the

annealing temperature. It suggests that the as-cast sample S25 contains the largest ΔV_f, and sample S380 has the least free volume left.

The two-point bending test and SEM were used to characterize the bending ductility and bent crease morphology of FeSiB alloy ribbons. The samples S25 and S250 show better bending ductility than S380. The bending strain of S25 and S250 both are 1 but S25 could be bent to a 180-degree angle about 10 times, and the bend times of S250 decrease to about 3 times. Meanwhile, the S380 exhibits no bending ductility and will be broken down in the initial stage of the bending test. Since the shear bands, owing to the plastic strain of amorphous alloy ribbons, could reflect the plastic deformation ability, a significant difference in shear band behavior can be noticed in Figure 4. S25 exhibits the most shear bands, followed by S250, and S380 shows the least. For S25 and S250, the shear bands are parallel to the bent crease and propagate in a normal direction to the bent crease. However, there are two obvious fracture edges and no shear bands for S380. The center area, where the distance is plus or minus 5μm from the bent crease, is selected to show the number of shear bands. For S25, the average number of shear bands is around 25, while it decreased to 5 for S250, then to 0 for S380. Moreover, several distinct cracks are produced in the bent crease for S250, suggesting decreased bending ductility, which is in agreement with the bending strain results.

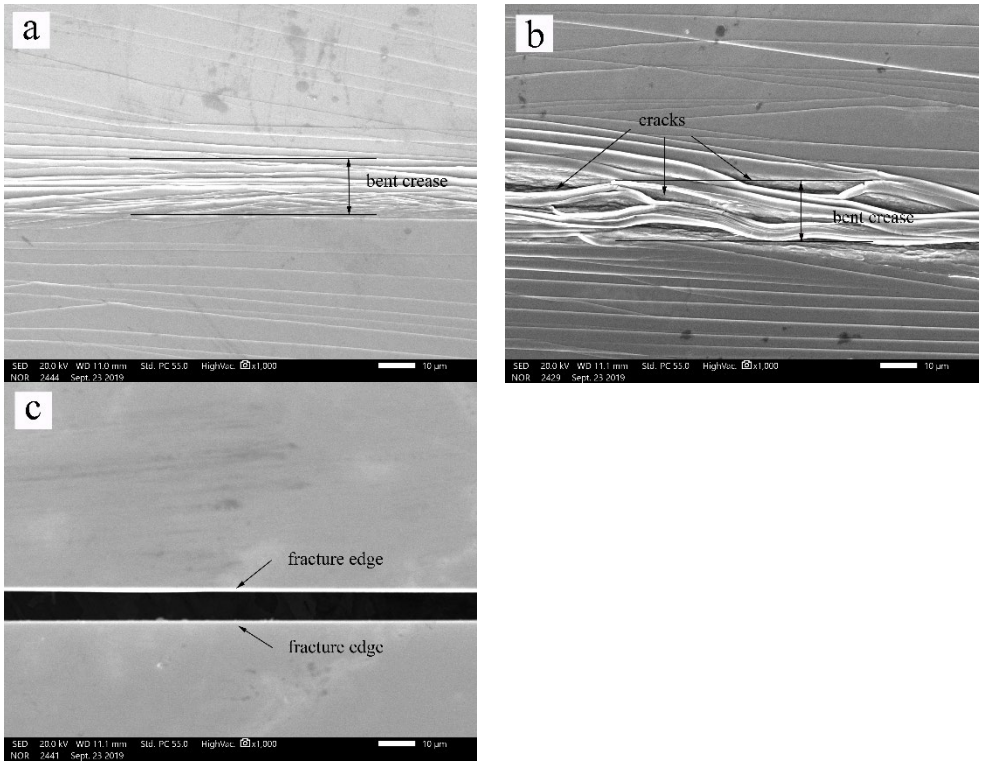


Figure 4. Shear band morphologies for amorphous alloy ribbons annealed at different temperatures: (**a**) S25; (**b**) S250; and (**c**) S380.

The fracture surface for the samples in different structure states was investigated with SEM, as shown in Figures 5–7. The fracture surface of S25 shows a periodic morphology consisting of a micro-scaled dimple pattern zone and the largest smooth zone, revealing ductile features (Figure 5a). The share of dimple pattern zone is up to 70%, the average dimple diameter is about 500 nm, and the smooth zone displacement is about 3.22 μm (Figure 5b,c). For S250, the fracture surface consists of a micro-scaled dimple pattern zone, smooth zone, and mist zone (Figure 6a), suggesting local ductile fracture. The share of dimple pattern zone decreases to 20%, the average dimple diameter is about 200 nm, and smooth zone displacement is about 1.52 μm (Figure 6b,d). At the microscale,

the fracture surface of S380 consists only of the smooth zone as shown in Figure 7a, suggesting a completely brittle fracture. From the high magnification image Figure 7b,c, both smooth zone and nanoscale configuration patterns appear on the fracture surface. The average dimple sizes further decrease to 100 nm and the smooth zone displacement is only about 500 nm (Figure 7b,d). The fractograph evolution from a micro-scaled dimple-like structure to a nano-scaled dimple-like structure and then to the periodic corrugation pattern along the crack propagation direction, indicates a ductile to brittle transition during the dynamic fracture process of S250. The fractograph of S380 consists only of the smooth zone. This means that the intrinsic plasticity of S250 and S380 have little resistance to crack propagation, and cracks will propagate rapidly throughout the whole sample until fracture once initiated. Together with the previous bending test, it can be concluded that the micro-scaled dimple pattern zone corresponds to the ductile feature, and those nano-scale dimples and periodic corrugations are typical fracture features of the quasi-brittle fracture of metallic glasses [15–18].

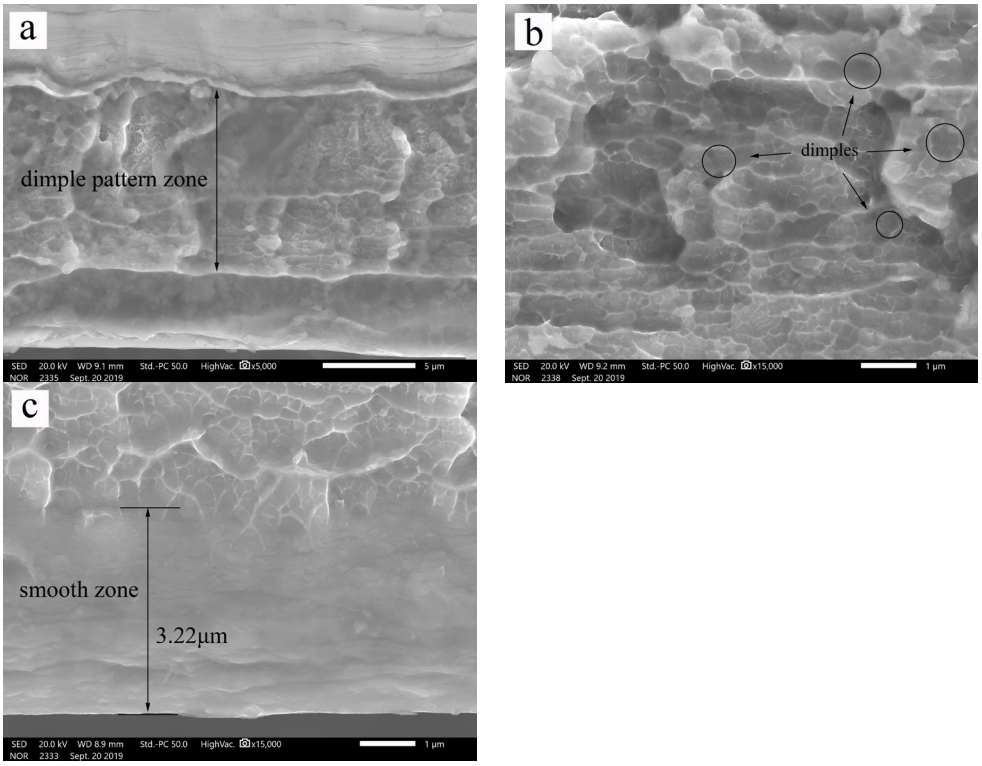


Figure 5. Fracture surfaces for S25: micro-scaled dimple pattern zone (**a**); enlarged images for dimple (**b**); smooth zone (**c**).

As reported, the size of STZ had been suggested as a key element in such plastic deformation [7,19,20]. The STZ volume, Ω, obtained by the rate-change method can be expressed as:

$$\Omega = kT/C'mH \tag{3}$$

where k is the Boltzmann constant, T is the temperature, H is the hardness, m is the corresponding strain rate sensitivity of hardness.

$$C' = \frac{2R\xi}{\sqrt{3}} \frac{G_0\gamma_C^2}{\tau_C} \left(1 - \frac{\tau_{CT}}{\tau_C}\right)^{1/2} \tag{4}$$

Here, $R \approx 1/4$ and $\xi \approx 3$ are constants, τ_c is the threshold shear resistance at temperature T and the $\tau_c/G_0 \approx 0.036$. The average elastic limit g $\gamma_c \approx 0.027$ and the value

of τ_{ct}/τ_c can be determined by $\tau_{ct}/G = \gamma_{c0} - \gamma_{c1}\,(T/T_g)^{2/3}$, where $\gamma_{c0} = 0.036 \pm 0.002$, $\gamma_{c1} = 0.016 \pm 0.002$ [21]. In order to obtain the STZ volume, calculating m is essential.

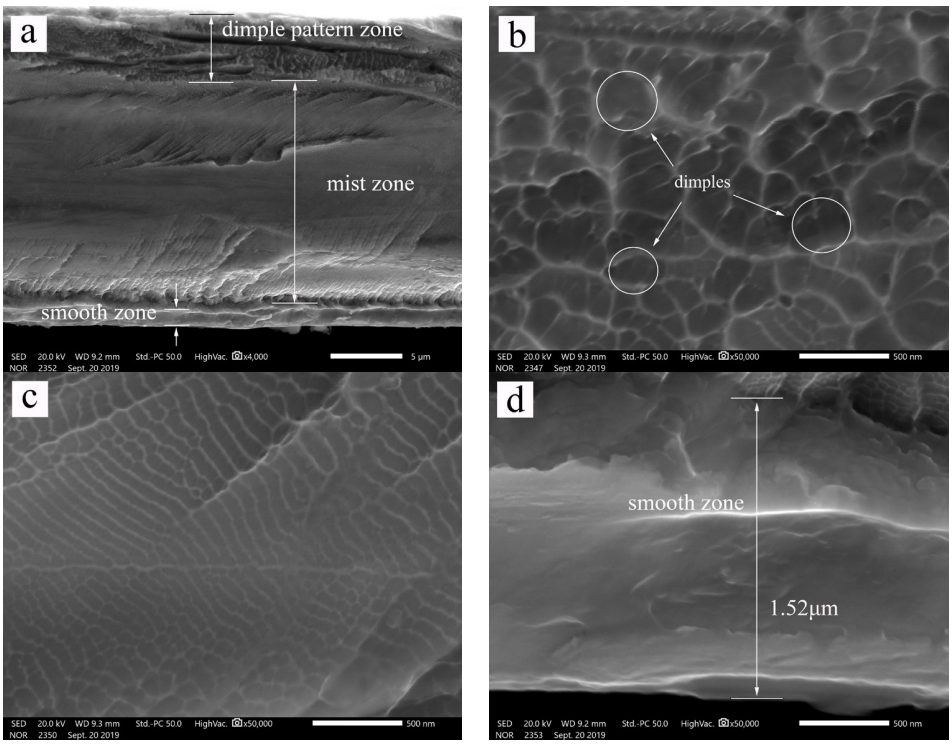


Figure 6. Fracture surfaces for S250: overview of fracture surface (**a**); enlarged images for dimple (**b**); mist zone (**c**); smooth zone (**d**).

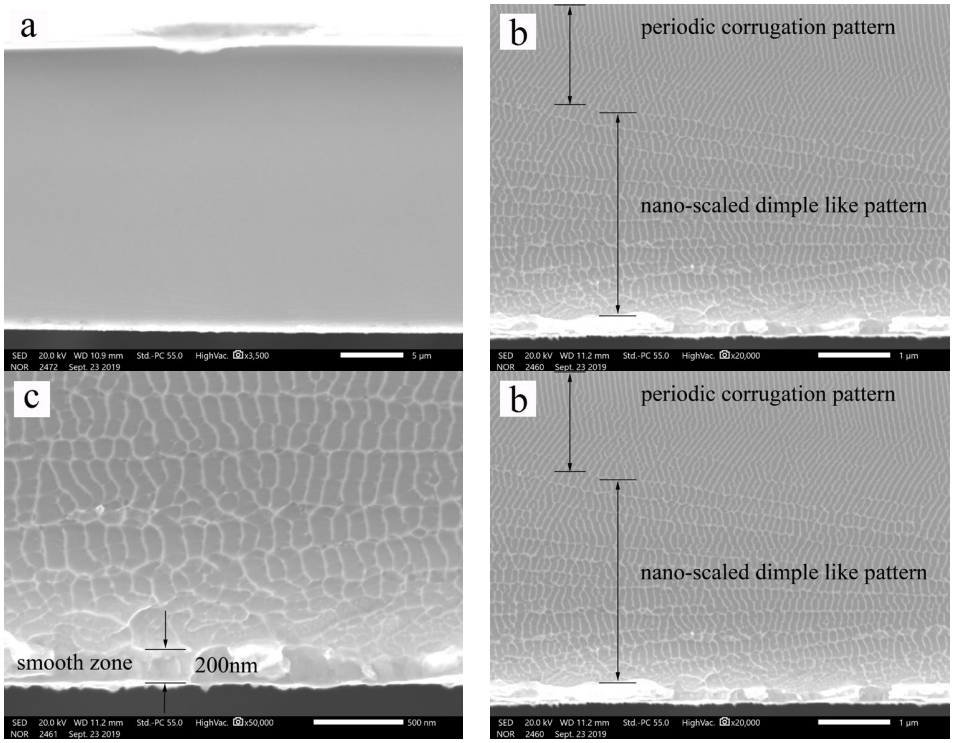


Figure 7. Fracture surfaces for S380: overview of fracture surface (**a**); enlarged images for nano-scaled dimple-like pattern (**b**); smooth zone (**c**); mist zone (**d**).

To investigate the changes in the bending ductility of FeSiB amorphous alloy ribbons after annealing treatment, nanoindentation experiments were conducted. The typical force-depth curves and hardness of S25, S250, and S380 by nano-indentation with a loading rate of 0.2 mN/s are shown in Figure 8. The maximum indentation depths for samples S380 and S25 were 52 nm and 75 nm, respectively. It was observed that the maximum indentation depth for S380 was significantly lower than that for S25, and the deformation rate of FeSiB amorphous alloy ribbons decreased continuously with increasing annealing temperature. In addition, the average hardness of S25 was 5.393 GPa, and the average hardness of FeSiB amorphous alloy ribbons increased continuously with increasing annealing temperature. Specifically, the average hardness of S250 and S380 increased to 6.992 GPa and 8.472 GPa, respectively. To calculate the value of m, the force-depth curves of S25, S250, and S380 by nano-indentation under loading rates of 0.01, 0.05, 0.1, and 0.2 mN/s are tested. According to Pan [9], the strain rate sensitivity m is proportional to the ratio of double log plot of strain rate $\dot{\varepsilon}$ to hardness H. The strain rate $\varepsilon = P/2P$, where P is the loading rate and P is the peak load force. The m values of as-cast, 250 °C annealed, 380 °C annealed samples are 0.340, 0.228, and 0.116 (as shown in Figure 9), respectively. In order to calculate the numbers of STZ, the atomic radius, based on the dense-packing hard-sphere model, can be computed as:

$$R = (\sum_i^n A_i r_i^3)^{\frac{1}{3}} \quad (5)$$

where A_i and r_i are the atomic fraction and atomic radius of each element, respectively [13]. The STZ volume, Ω, and the number of atoms, N, in the STZ are calculated and summarized in Table 1. It can be seen that U and N increase sharply with the annealing temperature. The Ω increases from 0.54 nm^3 for S25 to 0.63 nm^3 for S250 and 1.01 nm^3 for S380, respectively. The N, in the STZ of the S25, S250, and S380 is estimated to be 66, 76, and 123, respectively. It can be found that the variation tendency of N is the same as STZ volume. It has been accepted that densely packed atomic clusters and loosely packed liquid-like regions in amorphous alloys participate in plastic flow under deformation, which is thought to be the root of STZ events [12,22]. In general, the free volume will annihilate, liquid-like regions will be fewer and smaller in structural relaxation during the annealing process, and a more uniform and stable microstructure will be obtained. The liquid-like zones, in which the atom numbers could be changed under the stress, are able to participate in plastic flow, resulting in rising STZ events. Once an STZ forms, another one may generate in the neighborhood by the local strain field. As the stress spreads, more and more STZ would be activated until a shear band is created. In addition, the new STZs can be activated due to the larger local strain field caused by the adjacent shear band.

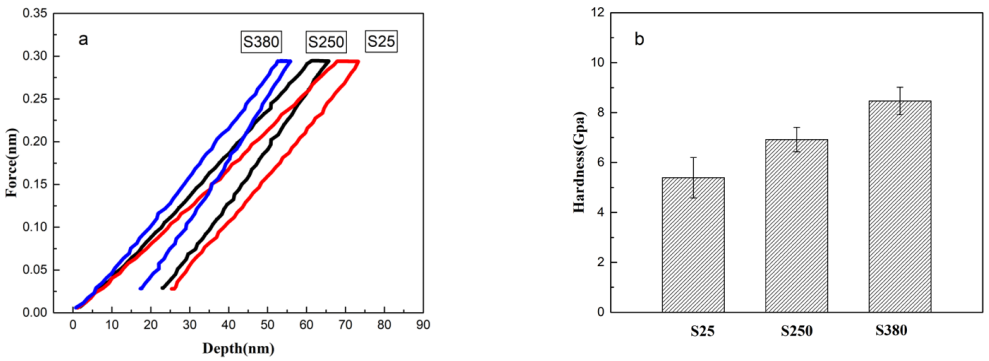


Figure 8. Force-depth curves (**a**) and hardness (**b**) of S25, S250, and S380 by nanoindentation with a loading rate of 0.2 mN/s.

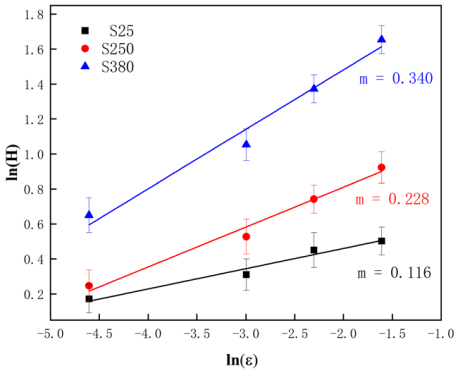


Figure 9. Determination of the strain rate of hardness(m) for S25, S250, and S380.

Table 1. The detailed measurement data on STZ for various samples.

Sample	Average Hardness H (Gpa)	Strain Rate Sensitivity, m	STZ Volume Ω (nm^3)	STZ Size N (Atoms)
S25	5.393	0.340	0.54	66
S250	6.922	0.228	0.63	76
S380	8.472	0.116	1.01	123

As reported, the larger Ω is, the less activated STZ is required to form a shear band [23]. In this study, S25 and S250 exhibit larger Ω and N, so more parallel and uniformly distributed shear bands in the bending crease exist in these two samples, showing better bending ductility.

During the bending process, the hydrostatic stress is max located on the tensile side of the ribbons, and the smooth region is formed by a sliding shear for crack nucleation occurring in shear bands.

At the prime stage of crack propagation, the crack tip slowly advances into the fracture process zone, and a large stress field is built. Once the crack length and the internal stress in the vicinity of the crack tip reach the critical value, the internal stress drives the crack to propagate in the adjacent area [24,25]. The amorphous matrix in front of the crack tip, containing numerous STZ and free volume, has enough time to rearrange. With the crack branching, the free volume supplies enough space for STZ rearrangement, and the dimple structure forms in the front of the crack tip. As a result, the periodical fatigue fracture characteristic forms on the fracture surface.

Thus, it can be noticed that the dimple patterns follow the smooth zone, but the radial dimple pattern of 3.3 μm for S25 decreases to 1.3 μm for S250 and then to 300 nm for S380. This may be attributed to the STZ volume and its correlation with the neighboring liquid-like areas in the plastic deformation zone ahead of the crack tips. Upon the long-range elastic field inducing the fluctuating internal stress and strain rate, larger STZ, more free volume, and liquid-like areas take part in the plastic flow and give rise to larger and deeper cavities. The largest critical shear displacement, dimple pattern size, and radial dimple pattern imply that S25 suffers lower crack propagation speed after crack initiation. The reduced critical shear displacement, dimple pattern size, and radial dimple pattern suggest that the crack propagation speed is not fixed. The crack propagation speed decreases along the crack propagation direction for S250. For the lowest STZ size and free volume in S380, the viscoelastic medium acts as an elastic-like deformation, and the internal stress is built up in the compressed viscoelastic medium. The STZ in the fracture process zone before the crack tip has no time to rearrange and the cavities are compressed. The nano-scaled dimple pattern appears instead of the micro-scaled dimple pattern. When the fracture zone is less than the wavelength of the meniscus instability, the dimple-like structure is suppressed and the periodic corrugation pattern appears.

4. Conclusions

In this work, the shear transformation zone and its correlation with fracture characteristics for Fe-based amorphous ribbons in different structural states were studied. Samples S25 and S250 show better bending ductility and the bending strains are both 1, while S380 exhibits no bending ductility. The shear band density decreases with the decrease in free volume. There are the most shear bands on the bent crease of S25. The fractograph evolution from a micro-scaled dimple-like structure to a nano-scaled dimple-like structure and then to the periodic corrugation pattern along the crack propagation direction, indicates a ductile to brittle transition during the dynamic fracture process for ductile samples. The fracture surface of S25 shows a micro-scaled dimple pattern zone and the largest smooth zone in these three samples, and the size of the dimple pattern zone is up to 70%. The corresponding part of S380 only consists of a smooth zone, suggesting a completely brittle fracture. The better bending ductility for S25 is attributed to the smaller STZ size. The nano-intention result indicates that the strain rate sensitivity of hardness, STZ volume, and the number of atoms in STZ increase after annealing. With the STZ volume increase, the fractograph evolution to a nano-scaled dimple-like structure and then to the periodic corrugation pattern along the crack propagation direction indicates that the amorphous alloy has become embrittlement.

Author Contributions: Conceptualization, W.D.; methodology, D.Q.; software, D.Q. and J.Z.; validation, W.D.; formal analysis, M.D. and J.Z.; investigation, W.D. and D.Q.; resources, S.Z.; data curation, W.D., M.D., J.Z. and S.Z.; writing—original draft preparation, W.D, M.D., D.Q., J.Z. and S.Z.; writing—review and editing, W.D. and M.D.; visualization, W.D.; supervision, W.D. and S.Z.; project administration, W.D. and S.Z.; funding acquisition, S.Z. All authors have read and agreed to the published version of the manuscript.

Funding: This work was supported by the Chinese Universities Scientific Fund (22D110323).

Institutional Review Board Statement: Not applicable.

Informed Consent Statement: Not applicable.

Data Availability Statement: Not applicable.

Conflicts of Interest: The authors declare no conflict of interest.

References

1. Minnert, C.; Kuhnt, M.; Bruns, S. Study on the embrittlement of flash annealed $Fe_{85.2}B_{9.5}P_4Cu_{0.8}Si_{0.5}$ metallic glass ribbons. *Mater. Des.* **2018**, *156*, 252–261. [CrossRef]
2. Liang, X.; He, A.; Wang, A.; Pang, J.; Wang, C.; Chang, C. Fe content dependence of magnetic properties and bending ductility of FeSiBPC amorphous alloy ribbons. *J. Alloys Compd.* **2017**, *694*, 1260–1264. [CrossRef]
3. Dong, W.; Han, B.; Hui, J.; Yan, M. Bending behavior and fracture surface characters for FeSiB amorphous ribbons in different free volume state. *Appl. Phys. A* **2020**, *126*, 670. [CrossRef]
4. Argon, A.S. Plastic deformation in metallic glasses. *Acta Metall.* **1979**, *27*, 47–58. [CrossRef]
5. Greer, A.L.; Cheng, Y.Q.; Ma, E. Shear bands in metallic glasses. *Mater. Sci. Eng.* **2013**, *R74*, 71–132. [CrossRef]
6. Narayan, R.L.; Raut, D.; Ramamurty, U. A quantitative connection between shear band mediated plasticity and fracture initiation toughness of metallic glasses. *Acta Mater.* **2018**, *150*, 69–77. [CrossRef]
7. Jiang, F.; Jiang, M.Q.; Wang, H.F.; Zhao, Y.L.; He, L.; Sun, J. Shear transformation zone volume determining ductile–brittle transition of bulk metallic glasses. *Acta Mater.* **2011**, *59*, 2057–2068. [CrossRef]
8. Pan, D.; Yokoyama, Y.; Fujita, T.; Liu, Y.H.; Kohara, S.; Inoue, A.; Chen, M.W. Correlation between structural relaxation and shear transformation zone volumeof a bulk metallic glass. *Appl. Phys. Lett.* **2009**, *95*, 141909. [CrossRef]
9. Pan, D.; Inoue, A.; Sakurai, T.; Chen, M.W. Experimental characterization of shear transformation zones for plastic flow of bulk metallic glasses. *Proc. Natl. Acad. Sci. USA* **2008**, *105*, 14769–14772. [CrossRef]
10. Ma, Y.; Ye, J.H.; Peng, G.J.; Wen, D.H.; Zhang, T.H. Nanoindentation study of size effect on shear transformation zone size in a Ni–Nb metallic glass. *Mater. Sci. Eng.* **2015**, *627*, 153–160. [CrossRef]
11. Choi, I.-C.; Zhao, Y.; Kim, Y.-J.; Yoo, B.-G.; Suh, J.-Y.; Ramamurty, U.; Jang, J.-I. Indentation size effect and shear transformation zone size in a bulk metallic glass in two different structural states. *Acta Mater.* **2012**, *60*, 6862–6868. [CrossRef]
12. Chen, Z.Q.; Huang, L.; Huang, P.; Xu, K.W.; Wang, F.; Lu, T.J. Clarification on shear transformation zone size and its correlation with plasticity for Zr-based bulk metallic glass in different structural states. *Mater. Sci. Eng. A* **2016**, *677*, 349–355. [CrossRef]

13. Ma, Y.; Peng, G.J.; Debela, T.T.; Zhang, T.H. Nanoindentation study on the characteristic of shear transformation zone volume in metallic glassy films. *Scr. Mater.* **2015**, *108*, 52–55. [CrossRef]
14. Slipenyuk, A.; Eckert, J. Correlation between enthalpy change and free volume reduction during structural relaxation of $Zr_{55}Cu_{30}Al_{10}Ni_5$ metallic glass. *J. Scr. Mater.* **2004**, *50*, 39–44. [CrossRef]
15. Raghavan, R.; Murali, P.; Ramamurty, U. On factors influencing the ductile-to-brittle transition in a bulk metallic glass. *Acta Mater.* **2009**, *57*, 3332. [CrossRef]
16. Xi, X.K.; Zhao, D.Q.; Pan, M.X.; Wang, W.H.; Wu, Y.; Lewandowski, J.J. Fracture of Brittle Metallic Glasses: Brittleness or Plasticity. *Phys. Rev. Lett.* **2005**, *94*, 125510. [CrossRef]
17. Jiang, M.Q.; Ling, Z.; Meng, J.X.; Dai, L.H. Energy dissipation in fracture of bulk metallic glasses via inherent competition between local softening and quasi-cleavage. *Philos. Mag.* **2008**, *88*, 407. [CrossRef]
18. Wang, G.; Zhao, D.Q.; Bai, H.Y.; Pan, M.X.; Xia, A.L.; Han, B.S.; Xi, X.K.; Wu, Y.; Wang, W.H. Nanoscale Periodic Morphologies on the Fracture Surface of Brittle Metallic Glasses. *Phys. Rev. Lett.* **2007**, *98*, 235501. [CrossRef]
19. Wu, F.F.; Zheng, W.; Deng, J.W.; Qu, D.D.; Shen, J. Super-high compressive plastic deformation behaviors of Zr-based metallic glass at room temperature. *Mater. Sci. Eng. A* **2012**, *541*, 199–203. [CrossRef]
20. Pan, D.; Guo, H.; Zhang, W.; Inoue, A.; Chen, M.W. Temperature-induced anomalous brittle-to-ductile transition of bulk metallic glasses. *Appl. Phys. Lett.* **2011**, *99*, 241907. [CrossRef]
21. Johnson, W.L.; Samwer, K. A universal criterion for plastic yielding of metallic glasses with a (T/Tg) 2/3 temperature dependence. *Phys. Rev. Lett.* **2005**, *95*, 195501. [CrossRef] [PubMed]
22. Liu, Y.H.; Wang, D.; Nakajima, K.; Zhang, W.; Hirata, A.; Nishi, T.; Inoue, A.; Chen, M.W. Characterization of nanoscale mechanical heterogeneity in a metallic glass by dynamic force microscopy. *Phys. Rev. Lett.* **2011**, *106*, 125504. [CrossRef] [PubMed]
23. Guo, W.; Yamada, R.; Saida, J. Rejuvenation and plasticization of metallic glass by deep cryogenic cycling treatment. *Intermetallics* **2018**, *93*, 141–147. [CrossRef]
24. Inoue, A.; Zhang, T.; Masumoto, T. Glass-forming ability of alloys. *J. Non-Cryst. Solids* **1993**, *156*, 598. [CrossRef]
25. Wu, F.F.; Zhang, Z.F.; Mao, S.X. Size-dependent shear fracture and global tensile plasticity of metallic glasses. *Acta Mater.* **2009**, *57*, 257. [CrossRef]

Disclaimer/Publisher's Note: The statements, opinions and data contained in all publications are solely those of the individual author(s) and contributor(s) and not of MDPI and/or the editor(s). MDPI and/or the editor(s) disclaim responsibility for any injury to people or property resulting from any ideas, methods, instructions or products referred to in the content.